Calculation of the electrical conductivity of strongly coupled plasmas

J. K. Yuan,[1,2] Y. S. Sun,[2] and S. T. Zheng[2]
[1]*Graduate School of China Academy of Engineering Physics, Institute of Applied Physics and Computational Mathematics, P.O. Box 8009, Beijing 100088, China*
[2]*Laboratory of Computational Physics, Institute of Applied Physics and Computational Mathematics P.O. Box 8009, Beijing 100088, China*
(Received 5 April 1995; revised manuscript received 13 July 1995)

The relativistic self-consistent average-atom model is employed to calculate the electrical conductivity of strongly coupled plasmas by using the extended Ziman formula. Calculation results for Fe plasma are compared with several theoretical models. For strongly correlated liquid metals, the electrical resistivities appear to be closer to the experimental data than that in G. A. Rinker, Phys. Rev. A **37**, 1284 (1988), since fully self-consistent potentials based upon solutions of the Dirac equation are used. The numerical results for Al plasma are largely consistent with the available experimental values [H. M. Milchberg *et al.*, Phys. Rev. Lett. **61**, 2364 (1988)]. Additional calculations show that contributions from the electron-ion inelastic scattering are negligible. Some results for Au plasma are also given for application.

PACS number(s): 52.25.Fi

I. INTRODUCTION

In recent years, the electrical conductivities of strongly coupled plasmas, produced by irradiating targets with high-power lasers or by imploding cylinders or wires, have been investigated [1–3]. A strongly coupled plasma can be defined by the coupling constant Γ ($=Z^2e^2/R_0k_BT$) when Γ is of order of unity or greater. $R_0=(3\Omega/4\pi)^{1/3}$ is the average separation between ions, where Ω is the atomic volume, which is determined by the density. As plasmas become dense, the mean kinetic and potential energies of particles are typically of the same order of magnitude. The microscopic dynamics of ions and electrons in strongly coupled plasmas are dominated by intensive interactions and a perturbation theory is no longer valid. There are many examples of strongly coupled plasmas. In the interiors of white dwarfs and Jovian planets, the coupling constant Γ varies in the range $10-10^3$. In laboratories strongly coupled plasmas can be created by exploding metal wires. The states of plasmas in the inertial confinement fusion (ICF) are similar to those in the solar interior. The temperature in ICF plasmas is of the order of 1 keV. The materials, which drive implosion of the fuel, consist of high-Z elements, such as Al, Fe, Au, and Pd. Under such high-temperature conditions, ionization occurs and a strongly coupled plasma with $\Gamma>1$ is formed. The design and numerical simulation of these experiments require transport coefficients over a wide range of temperature and density.

A number of authors have investigated the conductivity of hot dense plasmas in the strongly coupled region. Rinker [4,5] performed systematic calculations of transport coefficients for all the elements of the periodic table by using an extended Ziman formula. The electron scattering potential employed a model potential represented as a combination of Thomas-Fermi-Dirac (TFD) potential of high temperature and density and Hartree-Fock-Slater (HFS) potential for isolated ions. The cross sections for electron scattering were calculated by applying partial wave theory in order to avoid errors that may come from the Born approximation. The ion correlation was considered in the one-component plasma (OCP) approximation. Perrot and Dharma-wardana [6] used density-functional theory (DFT) to calculate the electron conductivity by employing the Ziman formula which extended from the weak-isolated-scatterer limit to the strong-multiple-scatterer limit. Ichimaru *et al.* [7] computed the conductivities of hot dense plasmas by using a general density-response formalism with inclusion of the various degrees of electron degeneracy and local-field correction. Some authors [8,9] used computer simulations to describe the transport properties of plasmas. A semiempirical method or a simple electron conductivity model is also very useful, because the complicated approaches require much computing expense and the practical application needs data over a wide range of the plasma's temperature and density. Mihajlov *et al.* [10] formulated a semiclassical theory for static conductivity and compared it with the quantum mechanical calculations in the random phase approximation (RPA). Lee and More [11] suggested a constructive conductivity model for hot dense plasmas which is based on the solution of the kinetic equation in the relaxation time approximation and modifying the Coulomb logarithm according to various regions in the phase diagram. Dharma-wardana and Perrot [12] first explored the effect of non-equilibrium between electrons and ions on resistivity in the view that the electron temperature can be much higher than the ion temperature for plasmas heated by laser pulses. In order to interpret experimental results, a more sophisticated model based on careful analysis of hydrodynamic expansion has been developed [13].

The electrical conductivity is very sensitive to the electron states. From gaseous, liquid plasmas to strongly

coupled plasmas, the electron states, including the ionization level, the binding energy level, and the mobility, change drastically. Therefore, it is very difficult to establish a single model that can describe the electron states of various plasmas. However, for strongly coupled plasmas, a simple muffin-tin (MT) potential model,

$$v(r)=\begin{cases}(\text{model potential}) & \text{for } 0<r<R_0\\ 0 & \text{for } r\geq R_0\end{cases},$$

can be employed to calculate the electrical conductivity, as successfully used in solid physics. This assumption correctly reflects the fact that the separation R_0 becomes the screening length in the strongly coupled region. As illustrated by Ref. [4], the predicted conductivity is found to be very sensitive to the detailed model potential. It is the model potential that determines the electron states, the electron-ion elastic scattering cross section, etc. In Rinker's work, the combination of TFD potential for high temperature and density and HFS potential for isolated ions is used as the model potential. This model potential is not self-consistent with the ionization degrees, bound states, chemical potentials, and scattering cross sections. In the present paper, we give up this assumption and use fully self-consistent potentials based upon the solution of the Dirac equation in the average-atom (AA) approximation [14,15]. The relativistic formulation is used so that the model can be applied in the case of heavy elements. We can expect that there will be a noticeable difference in the middle region but little difference in the two extreme cases. The results for Fe at 15 eV, 123 eV, and 1 keV for various densities confirm this conclusion.

The theoretical method is given in Sec. II. In the region of liquid states, the experimental data is well measured. In Sec. III, we first calculate the resistivity for liquid metals near the melting point to check the accuracy of this method, and then calculate the electron conductivity for Fe plasma and compare the results with other theoretical calculations. We also compare the results for Al plasma with available experimental values. For the application, we give some results for Au plasma.

II. THEORETICAL METHOD

In this section, we first give the extended Ziman formula and explain the quantities appearing in the formula, including the chemical potential, scattering cross section, and structure factor; then we briefly describe the relativistic self-consistent AA model to obtain all the required quantities. Atomic units are used except when a specific explanation is given.

The extended Ziman formula for the resistivity is given by [16]

$$\rho_e=\frac{4}{3\pi n_i Z_i^2 T}\int_0^\infty \varepsilon^2 f_\mu(\varepsilon)[1-f_\mu(\varepsilon)]\bar{\sigma}_\varepsilon d\varepsilon\ , \tag{1}$$

$$\bar{\sigma}_\varepsilon=16\int_0^1 \sigma_\varepsilon(q)a(q)x^3dx\ . \tag{2}$$

Here q is the transfer momentum, $x=q/\sqrt{8\varepsilon}$, $f_\mu(\varepsilon)$ is the Fermi-Dirac distribution, μ is the chemical potential, n_i is the average ion density, and Z_i is the average ionic charge. The structure factor $a(q)$ is used to specify the ion distribution. The differential cross section $\sigma_\varepsilon(q)$ for incident electron energy ε and momentum transfer q is used to describe the collisions between the moving electrons and ions. For the strongly coupled plasma, $\sigma_\varepsilon(q)$ should be obtained from the phase shifts of the scattering method. $\bar{\sigma}_\varepsilon$ can be regarded as the transport cross section, which includes the effect of ion structure.

In this paper, we use a simple analytic formula for the structure factor $a(q)$ which is based on the one-component plasma approximation. There exist many accurate methods to calculate $a(q)$, for example, the Monte Carlo (MC) method [17] and the calculations on the basis of the numerical solution of the hypernetted-chain (HNC) and modified HNC integral equations [18]. However, the strongly coupled plasma should be treated as a two-component plasma (TCP) consisting of ions and electrons. A two-coupled kinetic equation for electrons and ions has to be solved consistently, as DFT does. In order to avoid the complicated numerical calculation, we adopt the simple analytic express in Ref. [19], which can be compared with the numerical solution of the MHNC equation as well as the computer simulation data,

$$a(q)=\left\{1-\frac{3\Gamma}{q^4R_0^4\alpha_2^2}\left[\cos(qR_0\alpha_1)+2\cos(qR_0\alpha_2)-\frac{3\sin(qR_0\alpha_1)}{qR_0\alpha_1}\right]\right\}^{-1}, \tag{3}$$

where the parameter α_1 is mainly related to the height of the first peak of $a(q)$, whereas α_2 is related to the location of the peaks. The best value of α_2 is shown to be 1.45, while the parameter α_1 is found to be

$$\alpha_1=-0.1455\times10^{-2}\Gamma+0.9574$$

for Γ between 50 and 160 by adjusting expression (3) to the first peak of the structure factor tabulated by Rogers *et al.* [18]. For strongly coupled system, e.g., liquid metals at the melting point, the Percus-Yecick structure factor is adequate. For high temperature, the Debye-Huckel structure factor can be used.

Except for the structure factor $a(q)$, the remaining quantities in the Ziman formula can be achieved by using the relativistic self-consistent AA model. Here we give a brief description.

The AA model assumes that the electronic levels in the plasma are populated according to the Fermi-Dirac statistics:

$$b_j=g_j\{\exp[(\varepsilon_j-\mu)/T]+1\}^{-1}\ , \tag{4}$$

where b_j and g_j are the population and statistical weight of a single particle level ε_j with quantum number j, and μ is the chemical potential. The electronic potential is assumed to be spherically symmetric and the single particle wave functions satisfy the Dirac equation

$$\frac{dP(r)}{dr}+\frac{\kappa}{r}P(r)=\frac{1}{c}[\varepsilon+2c^2-v(r)]Q(r)\ , \tag{5}$$
$$\frac{dQ(r)}{dr}-\frac{\kappa}{r}Q(r)=-\frac{1}{c}[\varepsilon-v(r)]P(r)\ ,$$

where c is the speed of light, and the self-consistent potential $v(r)$ is given by

$$v(r)=-\frac{Z}{r}+\int d^3r'\frac{\rho(r')}{|r-r'|}+v_{xc}(r)\ , \tag{6}$$

where Z is the nuclear charge and the electron density is given by

$$\rho(r)=\rho_b(r)+\rho_f(r)\ , \tag{7}$$

$$\rho_b(r)=\frac{1}{4\pi r^2}\sum_j b_j[P_j^2(r)+Q_j^2(r)]\ , \tag{8}$$

$$\rho_f(r)=\frac{1}{4\pi r^2}\int_0^\infty f_\mu(\varepsilon)\sum_{\kappa=\pm1}^{\infty}2|\kappa|[P_\varepsilon(r)^2+Q_\varepsilon(r)^2]d\varepsilon\ , \tag{9}$$

where $\rho_b(r)$ and $\rho_f(r)$ are the bound and free electron density, respectively, $P_j(r)$ and $Q_j(r)$ are the bound wave functions, and $P_\varepsilon(r)$ and $Q_\varepsilon(r)$ are the continuum wave functions. To ensure the convergence, a large number of partial waves is required. Actually, in our calculations 100 partial waves are used. To speed up the calculation, we can use the TF approximation for the free electron density,

$$\rho_f(r)=\frac{1}{\pi^2}\int_{p_0(r)}^\infty p^2dp\{\exp[(\sqrt{p^2c^2+c^4}-c^2-v(r)-\mu)/T]+1\}^{-1}\ , \tag{10}$$

where $p_0(r)=[v^2(r)/c^2-2v(r)]^{1/2}$, which is determined by requiring the energy of a free electron to be no less than zero. Equation (10) is a good approximation because substantial deviations from Eq. (9) take place only near the ion. At large distance, they agree with each other very well. This will be shown in Sec. III B. For the exchange and correlation potential $v_{xc}(r)$, we adopt the formula of Dharma-wardana and Taylor [20].

For a given temperature, the chemical potential μ is determined by requiring charge neutrality in the ion-sphere:

$$4\pi\int_0^{R_0}\rho(r)r^2dr=Z\ . \tag{11}$$

Equations (3)–(10) give a complete self-consistent set of equations for the atomic structure of the AA model. The TF potential is used as the trial potential in the iteration processes. From the calculation, we can obtain the average ionic charge Z_i $(=Z-4\pi\int\rho(r)r^2dr)$, the chemical potential μ, the bound energy level ε_j, the self-consistent potential $v(r)$, and the electron distribution density $\rho(r)$. In Eq. (9), the resonance electrons of low-energy scattering are included. They are treated consistently in the iteration process. The AA model is very useful in dealing with the properties of plasmas, for example, in calculating the equations of state and the opacity in plasmas.

The effective scattering potential in the static approximation can be obtained from the electron density distribution, which is given as the muffin-tin potential form [21]

$$V(r)=\begin{cases}-\dfrac{Z}{r}+\displaystyle\int_0^{R_0}\frac{\rho(r')}{r_>}4\pi r'^2dr' & \text{for } 0<r<R_0 \quad (12)\\ 0 \quad \text{for } r\geq R_0 & (13)\end{cases}$$

where $r_>$ is the greater of r and r'. The gradient of $V(r)$ and itself are continuous at R_0. The assumption that the potential is zero outside the ion-sphere implies that the nucleus is completely screened by the electron cloud.

The scattering phase shift δ_k is calculated numerically by using the partial-wave expansion. In the interior region, which extends from $r=0$ to R_0, the continuum-state relativistic Dirac equation is solved numerically step by step. In the exterior region ($r>R_0$), the solution of the equation has an analytical form. The wave functions are

$$P_0(r)=\sqrt{\frac{\varepsilon+2c^2}{\pi kc^2}}kr[\cos\delta_k j_l(kr)-\sin\delta_k\eta_l(kr)] \tag{14}$$
$$=F_1(r)\cos\delta_k-F_2(r)\sin\delta_k\ , \tag{15}$$
$$Q_0(r)=\pm\sqrt{\frac{\varepsilon}{\pi kc^2}}kr[\cos\delta_k j_{l\mp1}(kr)-\sin\delta_k\eta_{l\mp1}(kr)] \tag{16}$$
$$=\pm[G_1(r)\cos\delta_k-G_2(r)\sin\delta_k]\ , \tag{17}$$

where the momentum k satisfies the dispersion relation $k^2c^2=\varepsilon(\varepsilon+2c^2)$. The upper (lower) sign is to be taken for the quantum number κ positive (negative). $j_l(kr)$ and $\eta_l(kr)$ are the spherical Bessel functions. $F_1(r)$, $F_2(r)$, $G_1(r)$, and $G_2(r)$ are the corresponding parts, except $\cos\delta_k$ and $\sin\delta_k$ in the first and second terms of $P_0(r)$ and $Q_0(r)$, respectively.

The phase shift δ_k is obtained by requiring that the two components of the Dirac equation be continuous at $r=R_0$. Therefore, the phase shift can be written as

$$\tan\delta_k=\left.\frac{P_iF_1-Q_iG_1}{P_iF_2-Q_iG_2}\right|_{R_0}\ , \tag{18}$$

where $P_i(r)$, and $Q_i(r)$ are the wave functions of the interior region. The finite temperature version of the Friedel sum rule is tested. Satisfaction of it shows that our calculations of phase shifts are correct.

For unpolarized incident electrons, the differential cross section is given by [22]

$$\sigma_\varepsilon(q)=|\sum_\kappa a_\kappa P_l(\cos\theta)|^2+|\sum_\kappa b_\kappa P_l^1(\cos\theta)|^2\ , \tag{19}$$

TABLE I. Resistivity for liquid metals at the melting point (T_M). Z_i, ρ(calc) are the present results. ρ_1, ρ_2 are from Ref. [5], which are calculated by using two choices of Z_i.

	D (g/cm^3)	T_M (eV)	Z_i	ρ(calc) ($\mu\Omega$ cm)	ρ_1 ($\mu\Omega$ cm)	ρ_2 ($\mu\Omega$ cm)	ρ(expt) ($\mu\Omega$ cm)
Fe	7.05	0.156	0.91	79.86	423	24	139
Co	7.72	0.152	0.902	77.56	281	9.1	102
Li	7.85	0.149	0.891	74.48	440	8.6	85
Cu	7.96	0.117	0.817	76.1	45	20	21
Zn	6.61	0.060	1.676	50.38	90	57	37
Al	2.385	0.08	1.066	16.001			24.3
Au	17.36	0.115	3.909	41.481			31

$$a_\kappa=\frac{1}{q}|\kappa|e^{i\delta_\kappa}\sin\delta_\kappa\ , \tag{20}$$

$$b_\kappa=\frac{1}{i\kappa}a_\kappa\ , \tag{21}$$

where θ is the scattering angle and $P_l(\cos\theta)$ and $P_l^1(\cos\theta)$ are the Legendre polynomial and the associated Legendre function, respectively. q is the momentum of the incident electron.

Until now, all the required quantities have been obtained. Therefore, one can calculate the electrical resistivity by using Eq. (1). In the actual application, the electron conductive opacity and the electron free path are needed. By using the Wiedemann-Franz formula, the relations with the electrical resistivity are

$$K_c=0.166\,42\frac{T^2}{D}\rho_e\ , \tag{22}$$

$$\bar{l}=\frac{1}{DK_c}\ , \tag{23}$$

where K_c is the electron conductive opacity, D is the density of the plasma, and $\bar{l}$ is the mean electron free path. The units for K_c, T, D, ρ_e, and $\bar{l}$ are cm^2/g, eV, g/cm^3, $\mu\Omega$ cm, and cm, respectively.

III. COMPARISON WITH OTHER THEORIES AND EXPERIMENTS

A. Results for liquid metals

In order to check the accuracy of this method, we calculate the resistivities for liquid metals near the melting point and compare with available measurements [5]. Results are shown in Table I. In the table, values of average ionic charge Z_i and resistivity ρ are the present calculations. ρ_1 and ρ_2 are from Ref. [5], which are calculated by using two choices of Z_i. We plot the results in Fig. 1. From the figure, we can see that the results of Ref. [5] have large discrepancy in comparison with the experimental data. The reason may be that the combination of TFD and HFS potential used in Ref. [5] is somewhat arbitrary. Our results appear to be closer to that of experiment. Since plasma conditions determine all quantities Z_i, μ, and $v(r)$ consistently and plasma conditions for liquid metals (Fe, Co, Ni, Cu) near the melting point are very similar, the results of resistivity have little difference among them. Therefore, the defect of this model can be seen, that is, the model cannot carefully distinguish the states of valence electrons. It is in our expectation since the atom model used is a statistical average atom model. More accurate treatment should employ detailed models, such as pseudopotential model, resonance model of s-d hybridization.

B. Results for Fe plasma

The theoretical method used in the present work is similar to Rinker's work, but the model potential is definitely different. In our calculations, the quantities Z_i, μ, $v(r)$, and $\rho(r)$ are fully self-consistent by solving the Dirac equation. There are two main differences between Rinker's model potential and ours. First, in our model potential the exchange and correlation energy have been included, which is usually very important in the calculation of atomic structure; second, the influence of bound states upon the model potential is considered consistently in the iteration. Therefore, we think the self-consistent potential would be more accurate under the validity of the AA model. In Fig. 2, we compare our results with other theories. From the figure, we can see our results agree with Rinker's very well at high temperature, 1 keV, but there are noticeable differences at relative lower temperatures, 123 and 15 eV. This is not surprising, since the AA model potential tends to the TFD potential at

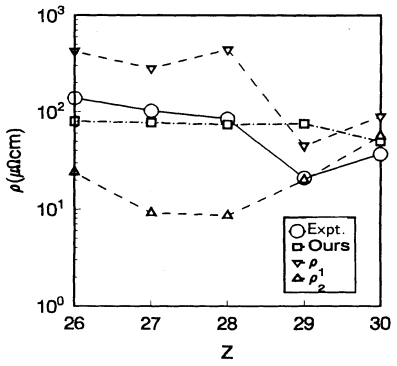

FIG. 1. Resistivities of liquid metals (Fe, Co, Ni, Cu, and Zn) near the melting point. ρ_1 and ρ_2 are from Ref. [5], which are calculated by using two choices of Z_i.

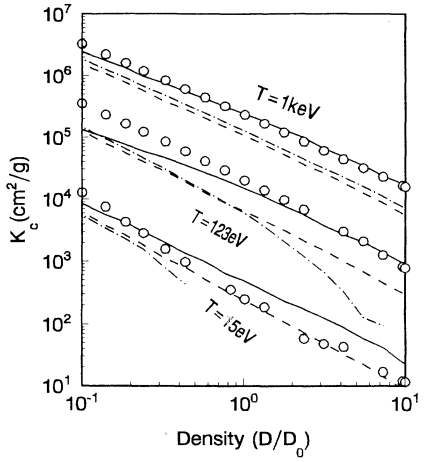

FIG. 2. Electron conductive opacity K_c versus density for Fe plasma at $T=15$, 123, and 1 keV. D_0 is the normal density (7.85g/cm^3). The circle is the present calculations. The solid line is Rinker's results in Ref. [4]. The dashed curve is the Sesame data [23]. The dot-dashed line is calculated from the Spitzer formula [24].

high temperature, but at the middle region, the self-consistent AA potential is surely different from the combination of TFD and HFS potential. From the figures, we can see the differences may reach a factor of 2. The Sesame data [23] and Spitzer results are also plotted in the figures for comparison, where in Spitzer formula [24] we make use of our calculation results for Z_i.

C. Results for Al plasma

Recently Milchberg *et al.* [1] have performed an experiment to measure the reflectivity of aluminum plasma at normal density in a wide range of temperature 0.1–100 eV. Many models [12,13,25] are employed to explain the experimental results. A very constructive model suggested by Dharma-wardana and Perrot [12] considers the effect of nonequilibrium since the electron temperature is different from the ion temperature. Ng *et al.* [13] present an interpretation based on careful analysis of hydrodynamic expansion and the nonlocal interaction of the incident laser field. Numerical simulation shows that an *ab initio* conductivity model [12] which is self-consistent gives the best agreement with the experiment. The method used in the present paper is similar to that in Ref. [6]; however, we pay more attention to the influence on the resistivity from the atomic structure and collision processes. We assume that the electrons and ions are in thermodynamic equilibrium. Under the experimental condition the ionic nonideality parameter Γ is greater than 1 and the Al plasma is strongly coupled. In this case, the MT potential model is a reasonable approximation, because at high density only the electrons near the nucleus feel the attraction due to the screening of the inner-shell electrons. The numerical results for the electrical resistivity comparing with the experiment [1] are plotted in Fig. 3. We can see that the quantitative picture of the electrical resistivity is correct. The results for

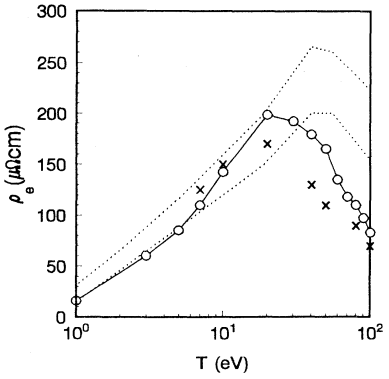

FIG. 3. Electrical resistivity for Al plasma versus electron temperature. The region bounded by two dotted curves shows the experimental data [1]. The circle sold line is our numerical results. The cross is read from Ref. [12], which is calculated for the nonequilibrium case.

$T<40$ eV agree well with the experiment values. A maximum and a downturn at $T=20$ eV appear, corresponding to an electron temperature of 40 eV according to the rescaled data [12]. For $T>40$ eV the results are approximately two times lower than the experiment. The results corresponding to the nonequilibrium dynamic resistivity of Dharma-wardana and Perrot [12] are also plotted in the figure. The same feature as discussed above appears. In view that the accuracy of the experiment results is within a factor of 2, our results are acceptable. Nevertheless, it is worthwhile to calculate carefully to see what happens in the calculation.

In Fig. 4, we give the free electron distribution for $T=40$ eV by using Eqs. (9) and (10). The profile resulting from Eq. (9) exhibits the well-known Friedel oscillations which vanish at large r, but the profile resulting from Eq. (10) is a smooth function of r. At large distance, we can see they are almost the same. This means that substantial deviations from TF uniform electron density distribution takes place only near the nucleus because of the influence of bound states.

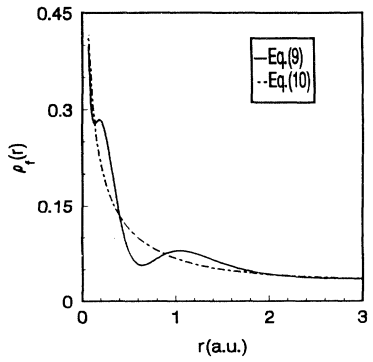

FIG. 4. Free electron distribution for Al plasma at $T=40$ eV. The solid line is calculated from Eq. (9), which exhibits the Friedel oscillation. The dot-dashed line is calculated from Eq. (10). They are almost the same at large r.

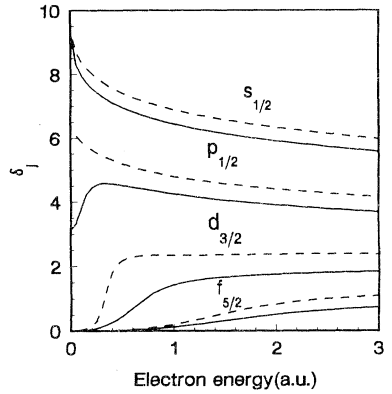

FIG. 5. Partial-wave phase shifts for aluminum plasma at $T=40$ eV (solid line) and $T=70$ eV (dashed line). The figure shows clearly that two resonance states, p wave and d wave, exist for $T=40$ eV while only one resonance state, d wave, exists for $T=70$ eV.

The electrons in the ion-sphere can be divided into three parts: bound, free, and resonance electrons. As bound states move into the continuum, the shape resonance occurs. The resonance electrons are neither strictly localized nor totally free; they contain a considerable amount of electrons moving largely in the vicinity of the nucleus. This may decrease the conductivity. In Figs. 5, 6, and 7, we give the phase shifts, state densities, and scattering cross sections, respectively, to understand the influence of the shape resonance upon the resistivity. For the perfect free electrons, the state density is $(\Omega/\pi^2)\sqrt{2\varepsilon}$. Figure 5 shows clearly that two resonance states, p wave and d wave, exist for $T=40$ eV, while only one resonance state, the d wave, exists for $T=70$ eV. Because of the shape resonance, the actual conductive electrons are less than the continuum electrons. For example, for $T=40$ eV, by integrating the area under the dashed and dotted

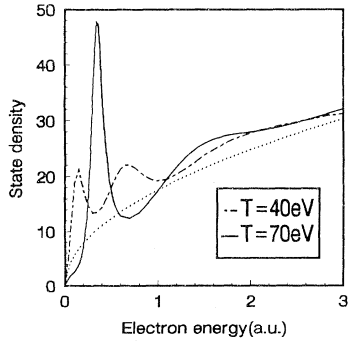

FIG. 6. Electronic density of states for aluminum plasma at $T=40$ eV (solid) and $T=70$ eV (dot-dashed). The state density of perfect free electrons is also plotted in the figure (dotted line). The two resonance peaks at $T=40$ eV correspond to the p and d resonance states, while the sharp resonance peak at $T=70$ eV correspond to the d state. The existence of resonance states causes the actual conductive electrons to be less than the continuum electrons.

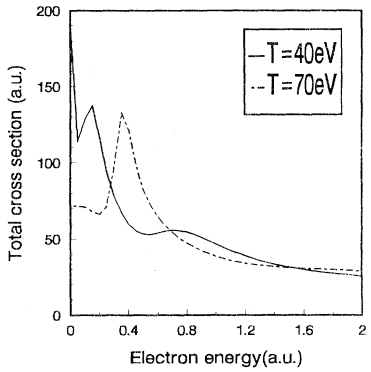

FIG. 7. Total scattering cross sections for Al plasma at $T=40$ and 70 eV. The shape resonances are exhibited as in Figs. 5 and 6. The resonance scattering increases the resistivity.

curves with a weighting factor $f_\mu(\varepsilon)$ in Fig. 6, we can find that the number of continuum electrons $\varepsilon>0$ is 5.2 while the number of actual conductive electrons is 3.3.

Although great efforts have been made in the calculations, the results for $T>40$ eV is lower than the experiment. This character can also be found in Refs. [12,25]. This makes us consider that there are other possible collision processes which may give large contributions to the resistivity under the assumption of the validity of this model. At high temperature, additional scattering processes (inelastic collision, ionization, recombination, and e-e interaction) occur which can reduce the mobility of the free electrons. In the present paper, only the e-i inelastic scattering is considered since contributions from the other three processes are very small [26].

As Ref. [27] did, the e-i inelastic scattering can be included in the extended Ziman formula by adding it to the elastic scattering. Thus, $\tilde{\sigma}_\varepsilon$ in Eq. (1) is substituted by

$$\tilde{\sigma}_\varepsilon=\tilde{\sigma}_\varepsilon^{el}+\tilde{\sigma}_\varepsilon^{\text{inel}}, \tag{24}$$

$$\tilde{\sigma}_\varepsilon^{\text{inel}}=\sum_{nj}\sum_{n'j'}P_{nj}\left[1-\frac{P_{n'j'}}{g_{j'}}\right]\times\sigma(nj-n'j'), \tag{25}$$

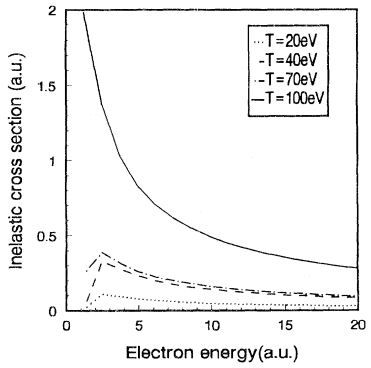

FIG. 8. Total inelastic cross sections for Al plasmas at various temperatures.

where $\tilde{\sigma}_\varepsilon^{\rm el}$ is the transport cross section, Eq. (2), and $\tilde{\sigma}_\varepsilon^{\rm inel}$ is the total excitation cross section. P_{nj} and $P_{n'j'}$ stand for the electron numbers in the shell of nj and $n'j'$. $g_{j'}$ is the statistical weight of final state $n'j'$. The factor $(1-P_{n'j'}/g_{j'})$ can be regarded as the availability factor of the level $n'j'$. The cross section for the $nj \rightarrow n'j'$ excitation induced by an incident electron having kinetic ener-

TABLE II. Resistivity values ($\mu\Omega$ cm) without (a) and with (b) the *e-i* inelastic collision. γ is the rate of increase.

	$T=20$ eV	$T=40$ eV	$T=70$ eV	$T=100$ eV
(a)	198.4	179.2	118.3	83.36
(b)	200.1	183.2	123.7	91.55
γ	0.86%	2.23%	4.56%	9.82%

TABLE III. Electron conductive opacity (K_c), mean free path ($\bar{l}$), chemical potential (μ), and mean ionic charge (Z_i) for Au plasma. $D_0=19.32$ g/cm^3.

D/D_0		0.01 keV	0.06 keV	0.1 keV	0.3 keV	0.7 keV	1 keV
0.01	K_c	8.453(4)	1.290(6)	2.232(6)	9.978(6)	4.452(7)	9.030(7)
	$\bar{l}$	6.123(−5)	4.012(−6)	2.319(−6)	5.187(−7)	1.163(−7)	5.732(−8)
	Z_i	4.001(0)	1.259(1)	1.923(1)	3.869(1)	5.534(1)	6.334(1)
	μ	−1.612(0)	−1.308(1)	−2.306(1)	−7.964(1)	−2.093(2)	−3.137(2)
0.06	K_c	7.457(3)	1.020(5)	2.338(5)	1.125(6)	3.065(6)	4.915(6)
	$\bar{l}$	1.157(−4)	8.454(−6)	3.690(−6)	7.667(−7)	2.814(−7)	1.755(−7)
	Z_i	3.664(0)	1.168(1)	1.637(1)	3.232(1)	4.928(1)	5.762(1)
	μ	−9.78(−1)	−9.281(0)	−1.705(1)	−6.185(1)	−1.662(2)	−2.513(2)
0.1	K_c	4.001(3)	5.205(4)	1.213(5)	6.072(5)	1.672(6)	2.552(6)
	$\bar{l}$	1.294(−4)	9.945(−6)	4.268(−6)	8.524(−7)	3.095(−7)	2.028(−7)
	Z_i	3.558(0)	1.107(1)	1.534(1)	3.078(1)	4.711(1)	5.541(1)
	μ	−7.96(−1)	−8.266(0)	−1.541(1)	−5.675(1)	−1.542(2)	−2.339(2)
0.3	K_c	8.028(2)	1.129(4)	2.814(4)	1.568(5)	4.560(5)	6.948(5)
	$\bar{l}$	2.149(−4)	1.528(−5)	6.132(−6)	1.100(−6)	3.783(−7)	2.483(−7)
	Z_i	3.385(0)	1.081(1)	1.402(1)	2.781(1)	4.305(1)	5.063(1)
	μ	−3.83(−1)	−5.86(0)	−1.166(1)	−4.571(1)	−1.282(2)	−1.969(2)
0.7	K_c	2.023(2)	3.618(3)	8.224(3)	5.363(4)	1.649(5)	2.516(5)
	$\bar{l}$	3.654(−4)	2.044(−5)	8.991(−6)	1.379(−6)	4.485(−7)	2.939(−7)
	Z_i	3.304(0)	1.076(1)	1.411(1)	2.603(1)	3.997(1)	4.744(1)
	μ	−2.92(−2)	−3.931(0)	−8.452(0)	−3.702(1)	−1.082(2)	−1.680(2)
1	K_c	1.340(2)	2.224(3)	5.234(3)	3.394(4)	1.063(5)	1.644(5)
	$\bar{l}$	3.861(−4)	2.326(−5)	9.888(−6)	1.525(−6)	4.871(−7)	3.148(−7)
	Z_i	2.682(0)	1.047(1)	1.359(1)	2.522(1)	3.907(1)	4.597(1)
	μ	−3.99(−2)	−3.156(0)	−7.230(0)	−3.338(1)	−9.959(1)	−1.560(2)
3	K_c	1.303(1)	3.367(2)	1.023(3)	7.842(3)	2.748(4)	4.334(4)
	$\bar{l}$	1.325(−3)	5.124(−5)	1.687(−5)	2.220(−6)	6.279(−7)	3.981(−7)
	Z_i	6.331(1)	1.151(1)	1.404(1)	2.3898(1)	3.589(1)	4.240(1)
	μ	1.365(0)	−1.32(−1)	−2.711(0)	−2.152(1)	−7.316(1)	−1.183(2)
6	K_c	1.823(0)	6.987(1)	2.662(2)	3.014(3)	1.144(4)	1.850(4)
	$\bar{l}_c$	4.731(−3)	1.235(−4)	3.241(−5)	2.862(−6)	7.542(−7)	4.663(−7)
	Z_i	1.034(1)	1.371(1)	1.553(1)	2.443(1)	3.448(1)	4.011(1)
	μ	3.159(0)	2.544(0)	8.47(−1)	−1.308(1)	−5.588(1)	−9.439(1)
8	K_c	3.129(−1)	4.169(1)	1.444(2)	2.035(3)	7.857(3)	1.290(4)
	$\bar{l}$	2.068(−2)	1.552(−4)	4.479(−5)	3.180(−6)	8.235(−7)	5.015(−7)
	Z_i	1.792(1)	1.312(1)	1.611(1)	2.385(1)	3.434(1)	3.957(1)
	μ	5.560(0)	3.436(0)	2.483(0)	−9.849(0)	−4.825(1)	−8.400(1)
10	K_c	7.457(3)	1.587(1)	7.445(1)	1.408(3)	5.816(3)	9.668(3)
	$\bar{l}$	1.157(−4)	3.262(−4)	6.953(−5)	3.675(−6)	8.900(−7)	5.354(−7)
	Z_i	3.664(0)	2.330(1)	2.417(1)	2.458(1)	3.451(1)	3.946(1)
	μ	−9.78(−1)	7.125(0)	6.167(0)	−6.655(0)	−4.205(1)	−7.560(1)

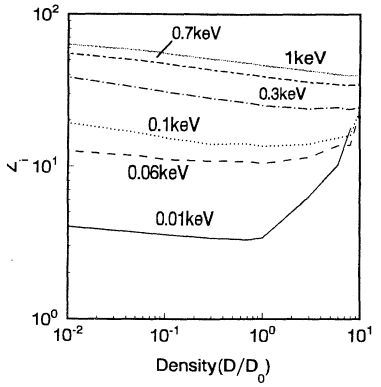

FIG. 9. Mean ionic charge as a function of temperature and density for Au plasma.

gy $\frac{1}{2}k^2$ in the first Born approximation is given by [28]

$$\sigma(nj-n'j')=\int d\Omega\frac{4\pi v}{Q^4 v'}|\langle n'j'|e^{i\vec{Q}\cdot\vec{r}}|nj\rangle|^2 , \quad (26)$$

where v and v' are the initial and final velocity of the incident electron. $\vec{Q}$ is the momentum transfer. The AA wave function is used to calculate the transition matrix element. More detailed information can be found in Refs. [29,30].

The total inelastic cross sections under various plasma conditions are given in Fig. 8. We can see that the inelastic cross section increases with temperature, but it is very small in comparison with the total elastic cross section (Fig. 7). In Table II, we give results without and with the *e-i* inelastic scattering contributions. It can be seen that the influence of the inelastic scattering is negligible, although the contribution increases with temperature. Reference [12] has reported the resistivity results which include nonequilibrium dissipative contributions, but they are still somewhat lower than the experimental data at high temperatures. The reason may be that the plasma model used to reduce the experimental data [1] become uncertain at high temperature, as stated in Ref. [12].

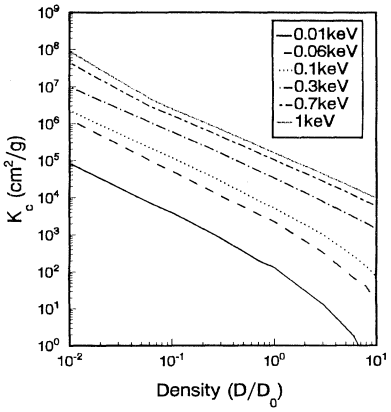

FIG. 10. Electron conductive opacity as a function of temperature and density for Au plasma.

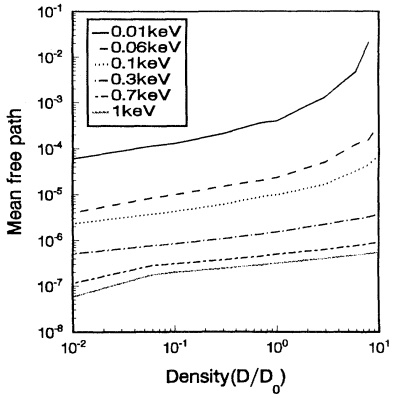

FIG. 11. Mean electron free path as a function of temperature and density for Au plasma.

D. Results for Au plasma

In the study of the laser-produced plasma, the electrical conductivity is required in performing the hydrodynamic simulation of the interaction of the target and laser ray. In Table III, we give some results of Au plasma for $T=0.01-1$ keV and $D=0.01-10D_0$ for application. Figures 9, 10, and 11 show that the mean ionic charge, the electrical conductive opacity, and the electron free path vary with the plasma's temperature and density. From Fig. 9, we can see that the thermal ionization dominates at relative lower density. As the density increases, the pressure ionization increases abruptly. At high temperature, the main ionization mechanism is thermal ionization. Figures 10 and 11 show that K_c and $\overline{l}$ vary almost linearly with density at high temperature.

IV. CONCLUSION

In the present work, we use the relativistic self-consistent AA model to calculate the electrical resistivity of strongly coupled plasmas. For liquid metals at the melting point, our theoretical calculations are more closer to experimental values than that in Ref. [5]. A comparison with Rinker's model potential for Fe plasma shows that the differences may reach a factor of 2 in the middle region of temperature and density. In order to investigate the validity of the model, we treat Al plasma carefully for comparison with the experiment results. The resonance state is treated strictly in the iteration process. We find the numerical results are in agreement with the experiment in view that the accuracy of the experiment is within a factor of 2. Calculation including the *e-i* inelastic collision shows that contributions from inelastic scattering are negligible. For application we give some results of Au plasma for $T=0.01-1$ keV and $D=0.01-10D_0$.

ACKNOWLEDGMENT

This work is supported by the National Science Foundation of China under Grant No. 19474008.

[1] H. M. Milchberg, R. R. Freeman, S. C. Davey, and R. M. More, Phys. Rev. Lett. **61**, 2364 (1988).
[2] Alan W. Desilva and H. J. Kunze, Phys. Rev. E **49**, 4448 (1994).
[3] J. F. Benage, Jr., W. R. Shanahan, E. G. Sherwood, L. A. Jones, and R. J. Trainor, Phys. Rev. E **49**, 4391 (1994).
[4] G. A. Rinker, Phys. Rev. B **31**, 4220 (1985).
[5] G. A. Rinker, Phys. Rev. A **37**, 1284 (1988).
[6] F. Perrot and M. W. C. Dharma-wardana, Phys. Rev. A **36**, 238 (1987).
[7] S. Ichimaru and S. Tanaka, Phys. Rev. A **32**, 1790 (1985).
[8] J. P. Hansen and I. R. McDonald, Phys. Rev. A **23**, 2041 (1981).
[9] David B. Boercker, Phys. Rev. A **23**, 1969 (1981).
[10] A. A. Mihajlov *et al.*, J. Phys. D **26**, 1041 (1993).
[11] Y. T. Lee and R. More, Phys. Fluids **27**, 1273 (1984).
[12] M. W. C. Dharma-wardana and F. Perrot, Phys. Lett. A **163**, 223 (1992).
[13] A. Ng *et al.*, Phys. Rev. Lett. **72**, 3351 (1994).
[14] B. F. Rozsnyai, Phys. Rev. A **5**, 1137 (1972).
[15] D. A. Liberman, Phys. Rev. B **20**, 4981 (1979).
[16] R. Evans, B. L. Gyorffy, N. Szabao, and J. M. Ziman, *The Properties of Liquid Metal* (Wiley, New York, 1973).
[17] W. L. Slattery, G. D. Doolen, and H. E. Dewitt, Phys. Rev. A **26**, 2255 (1982).
[18] F. J. Rogers, D. A. Young, H. E. Dewitt, and M. Ross, Phys. Rev. A **28**, 2990 (1983).
[19] J. L. Bretonnet and A. Derouiche, Phys. Rev. B **38**, 9255 (1988).
[20] M. W. C. Dharma-wardana and R. Taylor, J. Phys. C **14**, 629 (1981).
[21] J. K. Yuan, Y. S. Sun, and S. T. Zheng, J. Phys. B **28**, 457 (1995).
[22] N. F. Mott and Q. S. W. Massey, *The Theory of Atomic Collision* (Oxford University Press, London, 1965).
[23] Los Alamos Scientific Laboratory Report No. LALP-83-4, 1983 (unpublished).
[24] L. Spitzer and R. Harm, Phys. Rev. **89**, 977 (1953).
[25] A. Ya. Polishchuk *et al.*, Phys. Lett. A **157**, 406 (1991).
[26] W. Ebeling *et al.*, Trans. Prop. Dense Plasmas **47**, 109 (1984).
[27] E. E. Höhne and R. Redmer, Physica **128A**, 643 (1984).
[28] G. J. Hatton *et al.*, J. Phys. B **14**, 4879 (1981).
[29] J. K. Yuan, Y. S. Sun, and S. T. Zheng (unpublished).
[30] C. Blancard and J. Duban, Laser Part. Beams **12**, 401 (1994).